RESEARCH ARTICLE

Droplet WILEY

Digital twin of a droplet microarray platform: Evaporation behavior for multiple droplets on patterned chips for cell culture

Yanchen Wu[1,2] | Joaquin E. Urrutia Gomez[3] | Hongmin Zhang[1,2] | Fei Wang[1,2] | Pavel A. Levkin[3,4] | Anna A. Popova[3] | Britta Nestler[1,2,5]

[1]Institute for Applied Materials–Microstructure Modeling and Simulation, Karlsruhe Institute of Technology, Karlsruhe, Germany

[2]Institute of Nanotechnology, Karlsruhe Institute of Technology, Eggenstein-Leopoldshafen, Germany

[3]Institute of Biological and Chemical Systems (IBCS-FMS), Karlsruhe Institute of Technology, Eggenstein-Leopoldshafen, Germany

[4]Institute of Organic Chemistry, Karlsruhe Institute of Technology, Karlsruhe, Germany

[5]Institute of Digital Materials Science, Karlsruhe University of Applied Sciences, Karlsruhe, Germany

Correspondence

Fei Wang, Institute of Nanotechnology, Karlsruhe Institute of Technology, Hermann-von-Helmholtz-Platz 1, 76344 Eggenstein-Leopoldshafen, Germany.
Email: fei.wang@kit.edu

Anna A. Popova, Institute of Biological and Chemical Systems, Karlsruhe Institute of Technology, Hermann-von-Helmholtz-Platz 1, 76344 Eggenstein-Leopoldshafen, Germany.
Email: anna.popova@kit.edu

Abstract

Precise control of the evaporation of multiple droplets on patterned surfaces is crucial in many technological applications, such as anti-icing, coating, and high-throughput assays. Yet, the complex evaporation process of multiple droplets on well-defined patterned surfaces is still poorly understood. Herein, we develop a digital twin system for real-time monitoring of key processes on a droplet microarray (DMA), which is essential for parallelization and automation of the operations for cell culture. Specifically, we investigate the evaporation of multiple nanoliter droplets under different conditions via experiments and numerical simulations. We demonstrate that the evaporation rate is not only affected by the environmental humidity and temperature but is also strongly linked to the droplet distribution on the patterned surfaces, being significantly reduced when the droplets are densely distributed. Furthermore, we propose a theoretical method to aid in the experimental detection of volumes and pH variation of evaporating droplets on patterned substrates. This versatile and practical strategy allows us to achieve active maneuvering of the collective evaporation of droplets on a DMA, which provides essential implications for a wide range of applications including cell culture, heat management, microreactors, biochips, and so on.

Yanchen Wu and Joaquin E. Urrutia Gomez contributed equally to this study.

INTRODUCTION

The wetting phenomenon and evaporation of multiple droplets on solid surfaces are omnipresent in nature and technological applications.[1–3] In nature, for example, the raindrops impacting on the feathers of birds can be life-threatening due to the heat loss.[4] In applications, such as coatings,[5,6] microfluidics,[7,8] ink-jet printing,[9] and high-throughput assays,[10] precise control of the droplet shapes and the evaporation behaviors on heterogeneous surfaces is of fundamental importance.[11] Diverse strategies have been applied to manipulate the droplet morphology and to regulate the evaporation rate, among which micro- and nanostructured surfaces with tailored wetting properties are widely utilized.[12] For high-throughput assays, techniques such as lithography,[13] electrochemical deposition,[14] and chemical functionalization[15] are commonly used to design miniaturized and parallelized microarrays.

Use of microarray platforms, such as the droplet microarray (DMA), has shown that a combination of biocompatibility and miniaturization on hydrophilic and superhydrophobic micropatterns is capable of revolutionizing the area of "on-chip" analysis.[16,17] This is due to its intrinsic properties, such as increased spatiotemporal control, efficient generation of large amounts of data, reduced consumption of reagent and generation of waste, and enhanced versatility. These characteristics are due to the high level of customization, which can yield different sizes, shapes, and distributions of droplets on the DMA.[18]

Despite the advantages of miniaturization and parallelization, there are also limitations to the use of the DMA platform. Common laboratory procedures, such as temperature cycles, sample incubation, and microscopy steps, are extended from routinary tasks to complex operations. This is attributed to the significant increase in the evaporation rate as a result of the miniaturization of the platform itself. In addition, the presence of multiple droplets in array format results in a nonuniform evaporation effect. This phenomenon leads to a drop-to-drop variation in key parameters, such as reagent concentration, pH, and cell culture volume, causing a difficult-to-track bias in the final outcome.

To overcome this effect and have better control of the DMA platform, it is necessary to understand how wettability and environmental factors such as humidity and temperature impact the evaporation of the multiple droplets on patterned substrates. There have been a series of theoretical and experimental investigations focusing on interactions between multiple evaporating droplets in recent years.[19–27] Khilifi et al.[19] experimentally investigated the interaction between water drops deposited on a substrate and found that the variation of the droplet distance allowed control of the evaporation kinetics. Hatte et al.[20] theoretically and experimentally studied the evaporation lifetime for closely placed ordered linear droplet arrays and predicted the critical droplet separation length (droplet center-to-center distance) above which interfacial interaction ceases to exist. They found that when the ratio of the droplet separation length to the droplet equatorial diameter is greater than 2.6, the vapor-mediated interaction in the studied three-droplet

system can be neglected. Schofield et al.[21] theoretically studied the diffusion-limited evaporation of sessile droplets either singly or in pairs to quantify the shielding effect. They reported that the domain size considerably affects the lifetime of the droplets, but this conclusion is based on the evaporation of two-dimensional thin droplets. Wray et al.[22] proposed an asymptotic 3D model for predicting the evaporation of multiple sessile thin droplets in pairs and in a polygonal array. Based on this model, they theoretically predicted the "coffee ring" effect, which demonstrates quantitative agreement with the experimental results.[23] Chong et al.[24] demonstrated a new mechanism in a collective droplet dissolution process by considering the convection effect, which leads to different kinetics contrasting the shielding effect; the investigation was constrained to a constant contact angle of 90°. Edwards et al.[25] presented a simple interferometric technique to precisely measure the evaporation rate of a droplet array and they demonstrated that the evaporation rate is highly dependent on the droplet position within the array and the confinement of droplets. Masoud et al.[26] derived a theoretical model for the diffusive evaporation rates of multiple sessile droplets on a substrate and the findings are applicable to arbitrary contact angles and droplet spacing. In a recent study,[27] it was reported that for a droplet in arrays, the shielding effect cannot be neglected even when the spacing between the centers of two neighboring droplets is equal to 10 times the droplet base radius, which is different from the conclusion of Hatte et al.[20] mentioned above. The cutoff distance at which the shielding effect can be neglected is affected by a lot of influential factors that deserve to be explored further in depth.

The evaporation process is also affected by the contact line dynamics. There are two typical evaporation modes, namely, the constant contact radius (CCR) and the constant contact angle (CCA), which are determined by the wetting property of the surface. The droplets usually evaporate in a combined mode, or the so-called stick–slip mode, as reported in many studies.[28,29] For a diffusion-based evaporation, apart from the physical properties of the fluids and the initial distribution of vapor concentration, the evaporation rate is also highly dependent on the instantaneous droplet contact radius and the contact angle.[20] Hu et al.[30] proposed an approximate expression for the CCR mode evaporation of a sessile droplet with the contact angle ranging from 0° to 90°. In this model, an empirical function of the contact angle $f(\theta) = 0.27\theta^2 + 1.30$ was included, which is confirmed by the results from the literature. The contact radius and the contact angle can be obtained by analyzing the geometry of the droplet. However, the geometry of multiple droplets makes it a very challenging problem to solve. Previous studies mostly focused on droplets with circular contact lines; analytical studies of the evaporation of multiple droplets of other shapes due to the pinning effect are still limited.[31] Sáenz et al.[32] experimentally and numerically elucidated the evaporation of nonspherical droplets, albeit only the evaporation of a single droplet was considered. Here, we first propose a theoretical model to describe the single-droplet shape on chemically patterned substrates that have an array of hydrophilic spots surrounded by a superhydrophobic background (see the Supporting Information: Figure S1 for more information). The square

spot array was chosen for the study of the evaporation behaviors because it is most suitable for microscopy readouts due to the square field of view, while the circular configurations are used only for the pH experiments (see the Methods section for more details and information on the substrate formats of the DMA). This model enables precise description of the droplet shapes with sharp corners; thus, it is more accurate than other models when the droplet shape becomes anisotropic due to the wetting effect on the patterned surface.[33,34] Moreover, we develop a thermodynamically consistent model, the phase-field model,[35–37] which has been proven to be a robust method to handle the wetting problem and evaporation behaviors. Furthermore, we propose a concept to simultaneously detect the variation of the pH values of the droplet as a function of its volume. Our strategy offers essential guidelines for the development of a digital twin system for the DMA platform, whereby the experimental design on the DMA platform can be controlled, where steps such as conditions and the duration of the cell culture, sample preparation in droplets, microscopy steps, and others are very important for achieving robust results in miniaturized high-throughput screenings on a DMA chip.

The interaction of the digital twin and the physical twin on the DMA platform can be described as follows: experimental data from the physical twin, such as humidity, temperature, droplet base area, droplet height, and so on, are collected as input to feed into modeling of the digital twin. In the digital twin, the input data are evaluated, analyzed, and adapted through theoretical models and simulations conducted through the solver on the local personal computer or super computer. The collected data in the experiments are used to validate the models and identify the key influential factors for establishing the digital twin model, which accurately reflects the physical twin. Once the digital twin is established, the key parameters are varied to obtain predictions for the evolution of droplet shapes and volumes under different conditions. This serves as a guidance for the physical twin and provides insights into the optimization of experimental conditions on a DMA platform. The aim of establishing the digital twin for the DMA platform is to achieve precise control of the evaporation of multiple droplets on a DMA platform during experimental procedures.

RESULTS AND DISCUSSION

In the framework of the digital twin system, we use a phase-field model of Cahn–Hilliard (CH) type with a complex wetting boundary condition, which is formulated to include the Young's contact angle of a droplet on a chemically patterned substrate. The complex wetting boundary condition has been validated through experimental data and theoretical predictions in our previous work (see Refs. [38, 39] for the Allen-Cahn model and Ref. [40] for the Cahn-Hilliard model).

In the current model, we use a Dirichlet boundary condition with a constant composition $c = c_0$ on the vertical and top boundaries, which are far from the droplets, and thus c_0 corresponds to a certain environmental humidity. By changing c_0, evaporation occurs via diffusion. The driving force of the evaporation is the constant

chemical potential flux.[41] More details are presented in the Numerical model part of the Method section and the Supporting Information: Appendix. There are many other models that are used to address the complex phenomenon of droplet evaporation. We refer the reader to Cazabat and Guéna[42] and Semenov et al.[43] for more details. The present model is validated by simulating the evaporation of a single droplet confined within a square hydrophilic spot with a side length of 1 mm. The simulation results are compared with the experimental data. The droplet considered here is an aqueous solution of pure water with 5% glycerol vol/vol, which is referred to as "gly" throughout the manuscript. Glycerol was added to water to reduce the evaporation rate of the droplet during the experimental measurements so that the initial droplet height can be more easily controlled. Figure 1a,b shows, respectively, the simulation and experimental snapshots of a droplet evaporating under the humidity $H = 36\%$. During the evaporation process, the droplet fully occupies the hydrophilic spot, suggesting a CCR mode of evaporation. Additionally, we plotted the normalized height h/h_0 and the contact angle versus the evaporation time t (s) for this evaporating droplet, which is shown in Figure 1c, where the circles correspond to the experimental results and the solid lines depict the simulation results. It is found that the simulation results are consistent with the experimental data. It should be noted that we focus on the range for $h/h_0 > 0.1$ because at the final stage, the droplets become very small and the ratio of the interface width to the droplet size is relatively large, which may lead to lower accuracy of modeling. Moreover, in the final stage, the solution used in the experiments becomes thick and crystallization may occur, and the evaporation process is more complex than the initial stage. This complex process is beyond the scope of the present work. The relatively large deviation between the simulation and the experimental results of contact angles in the final stage can be explained as follows: in the present phase-field (PF) model, we only consider the diffusion process and we do not include fluid dynamics in the model. During the evaporation process in the simulations, the time scale for the surface tension effect and the fluid flow effect is assumed to be much larger than the time scale of the diffusion process, so that the droplet shape deviates a little bit from the equilibrium shape in the simulations. However, in real-world experiments, the droplet show adjustment of shape during the evaporation process through the fluid dynamics effect. On the other hand, there is a contact angle hysteresis effect caused by imperfections, such as surface defects or irregularities, which lead to the deviation of the contact angle and droplet shape. The overall good agreement between the simulation and experimental results reveals that the phase-field model developed in this work is robust and valid for describing the evaporation process of a single droplet on a chemically patterned DMA surface.

Similarly, as shown in Figure 2a, we conducted a series of single-drop evaporation experiments for solutions commonly used in laboratory applications, such as saline buffers and cell culture media with and without cells. Once the height evolution data were obtained, the normalized droplet height h/h_0 was plotted versus the nondimensionalized time $\tilde{t}$ represented by the different-colored
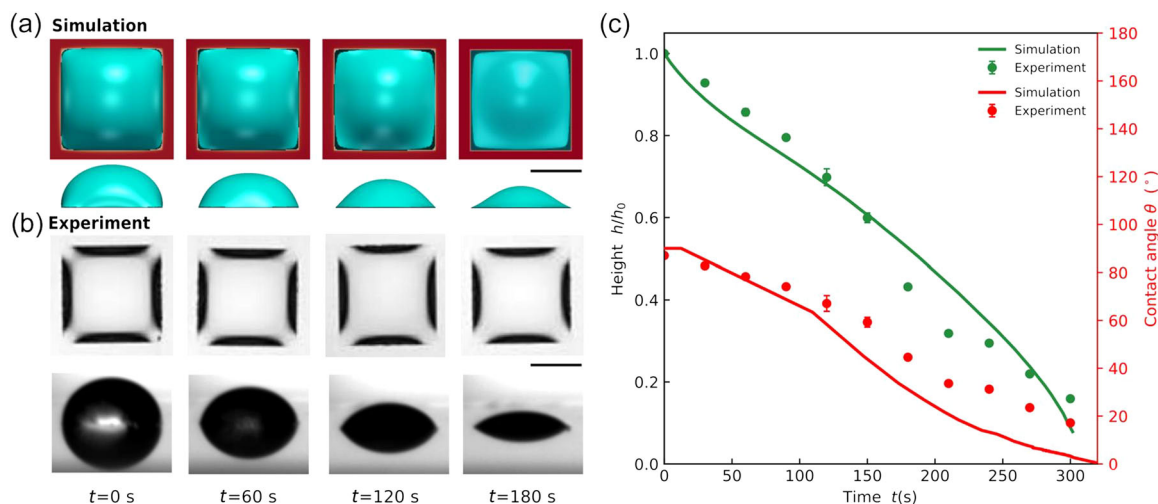
FIGURE 1 Comparison of simulation and experimental results for the evaporation process of a single gly-droplet on a square-patterned substrate. (a) The first and second rows show the top and side views for the simulated evaporating droplet at different times, respectively. (b) Corresponding experimental results. The squared spot is 1 mm^2 in size. During the evaporation process, the droplet fully occupies the hydrophilic spot, suggesting a constant contact radius (CCR) mode of evaporation. (c) Time evolution of the normalized droplet height h/h_0 and contact angle θ. Here, h_0 ($h_0 = 0.47$ mm) and h (mm) are the initial droplet height and the transient droplet height, respectively. The simulation results and experimental results are represented by the solid lines and dots with error bars. The coefficients of determination R^2 for droplet height and contact angle are 0.9582 and 0.7861, respectively. Scale bars: 0.5 mm.
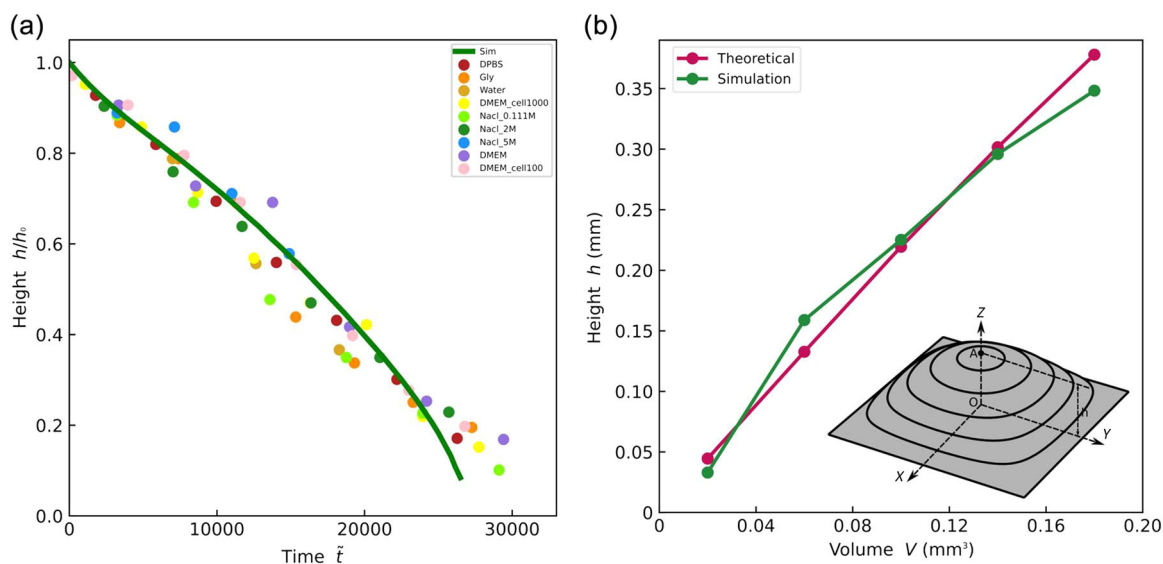

FIGURE 2 Analysis of the morphology of a single droplet on a square-patterned substrate. (a) Normalized droplet height h/h_0 ($h_0 = 0.47$ mm) as a function of nondimensionalized time $\tilde{t}$. The solid line denotes the simulation result and the colored circles indicate the experimental results obtained from different drop compositions. The coefficients of determination R^2 range from 0.9194 to 0.9910. (b) Droplet height as a function of volume for an equilibrium droplet on a square-patterned substrate. The red and green points show theoretical and simulation results, respectively. The coefficient of determination R^2 is 0.9696. The inset in (b) illustrates a schematic of an equilibrated droplet described by the theoretical model. The droplets in the simulations and the theoretical model fully occupy the superhydrophilic square spot, which is valid for all of the studied liquids in the considered volume range. Cell (100–1000), number of HeLa cells in the drop; DMEM, Dulbecco's modified eagle medium; DPBS, Dulbecco's phosphate-buffered saline; Gly, aqueous solution of pure water with 5% glycerol vol/vol; NaCl (0.1, 2, 5 M), sodium chloride at different molar concentrations in water; Sim, simulation.

circles. Here, the scaled time $\tilde{t}$ is given by $\tilde{t} = tD_e/x^{*2}$, with D_e (m^2/s) and x^* (m) denoting the effective diffusion coefficient and the characteristic length, respectively. More details of the nondimensionalization of the related variables are presented in the Supporting Information: Appendix section. The colored circles on the graph in Figure 2a collapse onto a master curve that coincides with the simulation result (solid curve). In the simulations, we solve the diffusion equations, revealing the diffusion-dominated nature of

the evaporation processes for the liquids considered in the current work. By comparing the simulations with the experimental results of distinct liquid solutions, the effective diffusion coefficient D_e is identified, as listed in Table 1. Note that the effective diffusion coefficient D_e used here is a modeling parameter in the simulation that is related to, but not the same as, the actual diffusion coefficient for system under investigation. The physical value describing the diffusion of one substance into the other is commonly determined experimentally.[44–46] In our investigation, we assume that the solution is dilute and the late stage of the evaporation is not our focus. Therefore, to simplify the model, the effective diffusion coefficient is assumed to be constant. The model for considering the transient behavior of the effective diffusion coefficient will be addressed in a forthcoming study. Among the liquid solutions listed in Table 1, water evaporates the fastest with the maximum D_e, while the aqueous solution of 5% glycerol evaporates at a relatively slower rate, showing smaller D_e. For the DMEM cell culture media, increasing the concentration of cells reduces the diffusivity, likewise increasing the concentration of NaCl in water.

Managing the evaporation phenomena on the DMA platform is very important, since the concentration of the solutes and the pH value in each individual droplet of cell culture media on the DMA are closely related to the droplet volumes. However, measuring the volume of a single droplet on a square spot over time is challenging.

To simplify this task, we propose an experimentally quantifiable theoretical model that relates the droplet volume to the droplet height. More details are described in the determination of droplet height versus volume part in the Method section. We describe the droplet shape by using a series of contour lines. The inset in Figure 2b illustrates a schematic of an equilibrated droplet described by the theoretical model. The functional relationship of droplet height versus volume predicted by the theoretical model is shown by the red line in Figure 2b, which is confirmed by the phase-field simulations (green line).

We further validated our phase-field model for simulating multiple droplets' evaporation against the experimental results. Figure 3a,b shows snapshots for the multiple droplet evaporation processes from phase-field simulations and experiments, respectively. The droplets in the center show a slower evaporation rate due to the presence of neighboring droplets, causing nonuniform evaporation. This phenomenon of nonuniform evaporation is caused by the heterogeneous distribution of the concentration of the vapor surrounding the droplets, known as the shielding effect.[21] Figure 3c quantitatively presents the evaporation processes (evolution of normalized height) for droplets at positions 1, 2, and 3, as highlighted in the first image of Figure 3a. The solid lines and circles show the simulation and experimental results, respectively. The results for the droplets at different positions are represented by different colors

TABLE 1 Effective diffusion coefficients D_e for different liquids determined by comparing experiments with phase-field (PF) simulations.

Liquids	Water	Glycerol	DMEM	DMEM^{100}	NaCl$^{0.1}$	NaCl^2	NaCl^5
$D_e/(10^{-8}$ m^2/s)	1.88	1.32	1.58	1.27	1.73	1.56	1.29
$D_e/D_{e,water}$	1.00	0.70	0.84	0.68	0.92	0.83	0.69

Note: The numeric index of Dulbecco's modified eagle medium (DMEM) represents the number of HeLa cells in the droplet; the indexes 0.1, 2, and 5 of NaCl represent the molar concentration per liter of pure water.
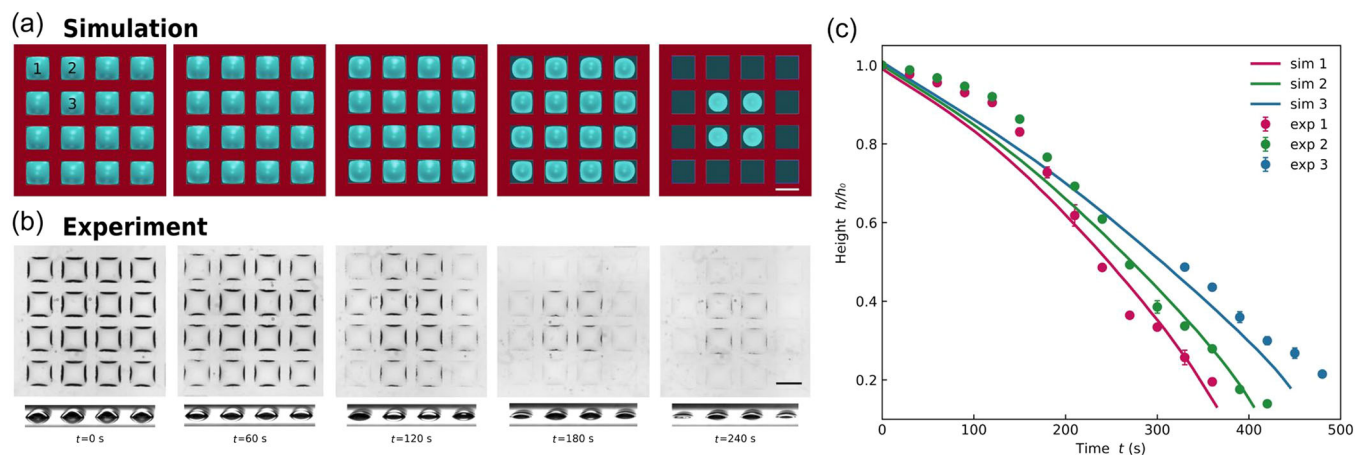

FIGURE 3 Comparison of the evaporation process for multiple droplets on a square-patterned substrate. The squared spots are 1 mm^2 in size arranged in a squared array 4 × 4 pattern configuration with edge-to-edge distance D = 0.5 mm. (a, b) Simulation and experimental results, respectively. (c) Time evolution of the normalized droplet height h/h_0 (h_0 = 0.47 mm) for the droplets at positions 1, 2, and 3, as highlighted in the first image of (a). The solid lines and circles show the simulation and experimental results, respectively. The results for the droplet at different positions are distinguished by different colors: 1, red; 2, green; 3, blue. The coefficients of determination R^2 for the results of droplets at positions 1, 2, and 3 are 0.9812, 0.9254, and 0.9533, respectively. Scale bars: 1 mm.

(1, red; 2, green; 3, blue). An excellent agreement between the simulations and experimental data was observed, and the shielding effect was successfully reproduced in the phase-field simulation. The deviations appearing at the early stages of evaporation are due to the fact that there is an accumulation of vapor phase surrounding the droplet array in the experiments when experimental observations were conducted, whereas in simulations, there is no accumulation of the vapor phase in the initial stage, so that the relatively low vapor concentration accelerates the evaporation in the simulations.

As a next step, we systematically studied the effects of humidity, temperature, and the distance between droplets on the evaporation process to achieve better control of droplet formation and evaporation behavior, aiming to provide important guidelines for the experimental design of miniaturized and parallelized experiments on the DMA. Figure 4a,b shows the evaporation processes (h/h_0 vs. t) under the humidity $H = 36\%$ for multiple droplets in 2×2 pattern and 4×4 pattern, respectively. In Figure 4a, the curves with different colors correspond to different distances (edge to edge) between the droplets D (mm). Due to the symmetric arrangement of the droplet position in the 2×2 pattern, the four droplets evaporate uniformly. It is further observed that as D decreases (from 0.5 to 0.2 mm), the normalized height h/h_0 of the droplets decreases more slowly, which are both slower than the single droplet, reflecting the decrease of the kinetics of droplet evaporation. A small distance between the droplets causes an enhanced shielding effect, due to the relatively higher local concentration of vapor, which slows the diffusion process of water from droplets to the surroundings. A similar effect is observed in Figure 4b for the case of the 4×4 pattern, albeit the evaporation kinetics for droplets at the positions 1, 2, and 3 are different. These are represented by the distinct types of lines in Figure 4b (see the inset figure in Figure 4b for the definition of droplet distance D and positions 1, 2, and 3). The droplets at position 3 (solid lines) evaporate slower than those at positions 1 and 2 (dashed lines) for both the studied distances D. Note that the curves for droplets at position 3 with different D (solid lines) diverge more than these for droplets at positions 1 and 2 (dashed lines). This
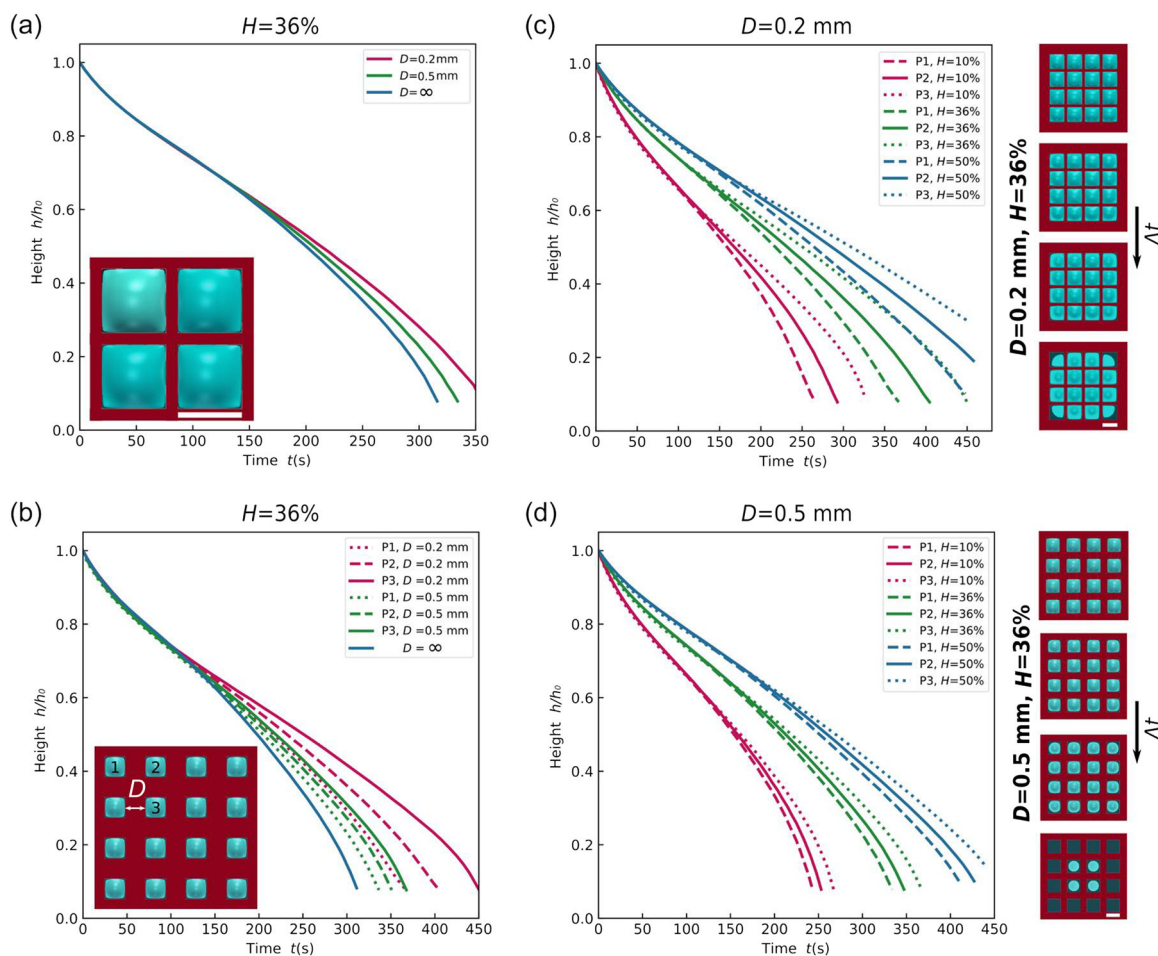

FIGURE 4 Simulation of the influence of the droplet distance D and humidity H on the evaporation process. (a, b) Time evolution of the normalized droplet height for the evaporating droplets under the same humidity $H = 36\%$ but with different droplet distances. Initially, we consider 4 (in 2×2 pattern) and 16 (in 4×4 pattern) sessile droplets with the same height $h_0 = 0.47$ mm in (a, b), respectively. $D = \infty$ denotes the result for single-droplet evaporation. (c, d) Evaporation behaviors for the 16 droplets under different humidities but with a certain droplet distance ([c] $D = 0.2$ mm; [d] $D = 0.5$ mm). The snapshots next to the plot diagrams denote the top views of the evaporating 16 droplets under the humidity $H = 36\%$ with the corresponding droplet distances. Scale bars: 1 mm.

reveals that droplets at position 3 are more sensitive to the variation of D than droplets at positions 1 and 2. In addition, as D increases from 0.2 to 0.5 mm, the curves for the evaporating droplets at different positions become less divergent (see the differences in the red and green curves in Figure 4b, respectively). It is anticipated that uniform evaporation can be observed for a very large value of $D = \infty$, which shows the same evaporation kinetics as a single droplet with the fastest evaporation behavior (blue solid line in Figure 4b), whereas nonuniform evaporation occurs for small values of D, such as $D = 0.2$ and 0.5 mm.

Apart from the position of the droplet within the array and the distance between the droplets, the environmental humidity H is an important factor influencing evaporation behaviors. Figure 4c,d shows the influence of the environmental humidity on the evaporation process of multiple droplets in 4×4 pattern with $D = 0.2$ and 0.5 mm, respectively. In each diagram, the results for droplets at different positions are distinguished by different types of lines, whereas the results for droplets under different environmental humidities are distinguished by different colors (red: $H = 10\%$, green: $H = 36\%$, blue: $H = 50\%$). It is found that a decrease in the environmental humidity remarkably accelerates the evaporation process. However, the three groups of evaporation curves for droplets at different positions but under the same environmental humidity (either in red, blue, or green) diverge almost to the same extent. This reveals that environmental humidity has a minor influence on the shielding effect. The extent of divergence of the evaporation curves with the same color (i.e., under the same humidity) is merely dependent on the droplet distance D. In summary, the evaporation rate is closely related to the environmental humidity, but the difference between the evaporation rates of droplets at different positions is affected by the droplet distance, since the shielding effect is more related to the local humidity than environmental humidity. This shielding effect can be weakened by increasing the droplet distance.[20-22] For a very large drop-to-drop distance, the shielding effect can be neglected to guarantee ideal parallelization on the DMA. However, due to the limitation of computational load for a very large domain, this cutoff distance is not the focus of our current work. Nevertheless, the shielding effect slows down the evaporation, which is beneficial for establishing a stable culture environment.

To examine evaporation under different temperatures, our model was extended by relating the effective diffusion coefficient D_e to temperature T (K) as[47]

$$D_e = \frac{0.01498T^{1.81}(1/M_A + 1/M_B)^{0.5}}{P(T_{cA}T_{cB})^{0.1405}(V_{cA}^{0.4} + V_{cB}^{0.4})^{0.5}}, \quad (1)$$

where, P (N/m^2) is the pressure. The parameters M_i (g/mol), T_{ci} (K), and V_{ci} (m^3/mol) are the molecular weight, the critical temperature, and the critical molar volume of component i ($i = A, B$), respectively. In the studied system in this work, we assume that the temperature and the pressure change within a small range. Thus, parameters P, M_i, T_{ci}, and V_{ci} are constant values; therefore, we have $D_e \propto T^{1.81}$. Based on the value of D_e at room temperature $T = 298$ K, we can calculate D_e

for other temperatures. It should be noted that in the literature, there are many other empirical equations relating the effective diffusion coefficient D_e with temperature T, which are closely tied to the experimental observations of the studied material system.[44-46] Here, we show the concept of extending the phase-field model by adopting the empirical equation that is supported by experiments. The empirical equation implemented within the phase-field model is the key parameter that decreases the gap between the real DMA platform (physical twin) and the digital twin.

As a main goal of creating a DMA digital twin, we have utilized our model for describing a real-life wet lab application case. Figure 5a shows the simulation of the evaporation kinetics of a single droplet of DMEM cell culture media on a square pattern. In this simulation, it can be observed how the droplet is exposed to a simulation of different typical experimental conditions like temperature and humidity, which correspond to refrigeration, incubation steps, and manipulations at room temperature. The solid black line denotes the evolution of the normalized volume V/V_0 under the conditions with the given temperature and humidity at different time intervals, as highlighted in different colors in Figure 5a, while the dot-dashed red line represents how the concentration of solutes (e.g., cell culture media components, or drugs in screening applications) varies as the volume changes, and this concentration change is calculated using the dilution equation $c_{d1}V_1 = c_{d2}V_2$ and the equation $Rc_d = (c_{d2} - c_{d1})/c_{d1}$ at each point. Here, c_{di} (mol/m^3) and V_i (m^3) are the concentration of the drug-screening molecule and droplet volume at time point t_i with $i = 1$ or 2. Rc_d represents the corresponding concentration increase rate. As reference lines, the dashed green line indicates the theoretical prediction for the evolution of V/V_0 for droplets under the combined conditions of the given temperature and humidity at different stages, while the black dashed line represents the evolution of the normalized volume V/V_0 for droplets under a constant condition of $H = 50\%$ and $T = 25°C$. The theoretical prediction is based on the diffusion-based evaporation model,[20,30] which assumes that the rate of droplet volume change $\dot{V}_{sim}$ (m^3/s) is proportional to the effective diffusion coefficient D_e, droplet base radius R_b (mm), vapor concentration difference near and far from the interface Δc, and geometric factor $f(\theta)$, which is related to the contact angle, that is, $\dot{V}_{sim} \propto D_e R_b f(\theta) \Delta c$. In the whole evaporation process, the droplet base radius R_b is constant, Δc is proportional to the relative humidity H, and the effective diffusion coefficient D_e for different temperatures can be calculated according to the relation $D_e \propto T^{1.81}$. To simplify the influence of the contact angle, we use $f_1(\theta)$ and $f_2(\theta)$ to describe geometric factors for large contact angles ($V/V_0 \geq 0.3$, $t = 0-184$ s) and small contact angles ($V/V_0 \leq 0.3$, $t = 184-326$ s), respectively. By fitting the evaporation rates at two typical time intervals $t = 76-110$ s (for large contact angles) and $t = 184-256$ s (for small contact angles) with the simulation results, we can calculate the evaporation rates at other time intervals, as listed in Table 2. In Table 2, the simulated volume change rates at different time intervals are also listed, which show good agreement with the theoretical predictions. The dashed green line in Figure 5a is obtained by assuming the same initial volume as in the simulation and using the theoretically predicted
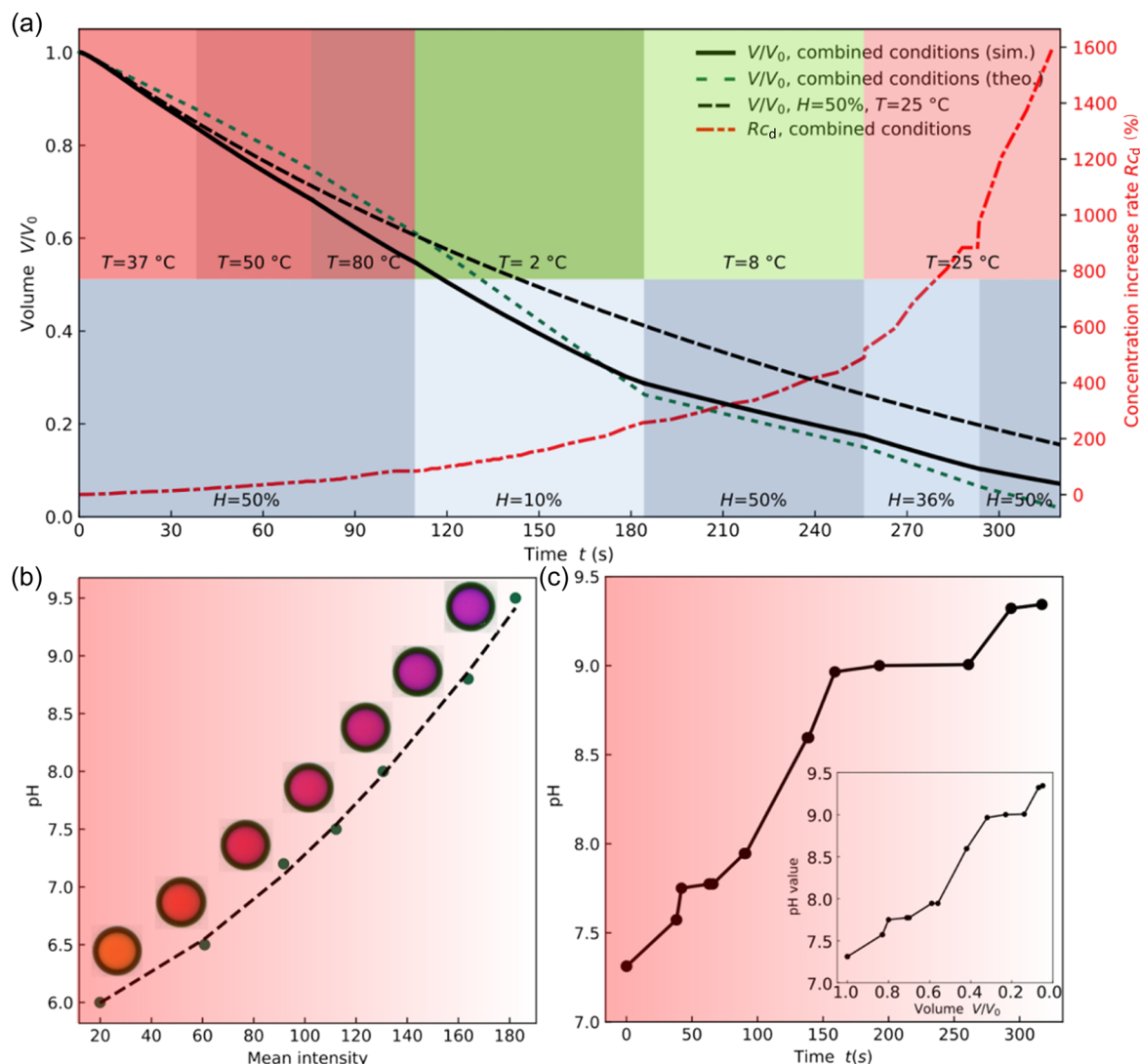
FIGURE 5 Combined influence of temperature T and humidity H and monitoring of droplet pH. (a) Simulation of the evaporation dynamics for a single droplet on a square-patterned substrate under different T and H. Droplets of Dulbecco's modified eagle medium (DMEM) cell culture media are considered. The solid black line represents the simulation result under conventional laboratory conditions with the given temperature T and humidity H at different stages, which are highlighted by different colors. The dashed green line reflects the theoretical prediction under the same conditions. The dot-dashed red line represents the concentration change rate of a solute (e.g., cell culture components, drugs, and compounds) under the same conditions. $T = 37°C$; $H = 50\%$: droplets exposed to cell culture incubator conditions. $T = 50°C/T = 80°C$; $H = 50\%$: heating process for cell lysis by thermal shock. $T = 2°C$; $H = 10\%$ and $T = 8°C$; $H = 50\%$: cooling process to complete the cell lysis mediated by thermal shock. $T = 25°C$; $H = 36\%$: the conditions for manipulation of the samples after undergoing thermal shock. Specifically, this involves performing cell lysis control under a microscope. $T = 25°C$; $H = 50\%$: the microenvironment within the liquid printer to print new reagents in each droplet. The black dashed line indicates a reference simulation result under $H = 50\%$ and $T = 25°C$. (b) Functional relationship between the mean intensity of the droplet color and the pH value. The pH values for droplets with different volumes are individually measured in experiments. The fitting function is indicated by the dashed line and the coefficient of determination R^2 is 0.9973. (c) Evolution of the pH value during the droplet evaporation process. The initial state of the evaporating droplet corresponds to the third case from (b), with pH = 7.3. The measured pH values are based on the intensity measurement. The inset shows the functional relationship between pH value and droplet volume.

evaporation rates in Table 2. From 0 to 110 s, the humidity for the solid black and dashed black lines is the same but the temperature for the solid black line is higher than that of the dashed black line. In this case, the solid black line decreases slightly more quickly due to the heating effect. The similar change of volume in time for the heated cases, especially at $T = 37°C$ and $50°C$, when compared to the dashed black line ($T = 25°C$) is due to the delayed response in the evaporation

process when switching from different temperatures. The delayed response occurs because the transport of the vapor phase needs some time to establish a new quasi-static evaporation state for a new condition of the given temperature and humidity. Later on (from 110 to 184 s), although there is a cooling effect at $T = 2°C$, the solid black line declines even more quickly than the dashed black line because the very low environmental humidity ($H = 10\%$) for the solid black line

TABLE 2 Evaporation rates obtained from simulation results $\dot{V}_{sim}$ and theoretical predictions $\dot{V}_{theo}$ under conventional laboratory conditions with the given temperature T and humidity H at different time intervals.

Time intervals	0–38 s	38–76 s	76–110 s	110–184 s	184–256 s	256–293 s	293–326 s
Conditions (T; H)	37°C; 50%	50°C; 50%	80°C; 50%	2°C; 10%	8°C; 50%	25°C; 36%	25°C; 50%
$\dot{V}_{sim}/(10^{-3}$ mm^3/s)	4.95	4.95	4.81	4.19	1.87	2.23	1.43
$\dot{V}_{theo}/(10^{-3}$ mm^3/s)	3.80	4.10	4.81[a]	5.51	1.87[b]	2.66	2.07

Note: The theoretical results for the evaporation rates labeled by indexes a and b include fitting values from the simulations for large and small contact angles, respectively. The time intervals 0–184 and 184–326 s correspond to large and small contact angles, respectively.

predominantly drives the diffusion process. Thereafter, from 184 to 256 s, with the same humidity but lower temperature, the solid black line declines slightly slower than the dashed black line, showing a pure cooling effect. From 256 to 293 s, the solid black line declines slightly quicker due to the lower humidity. In the final stage, the two curves have the same temperature and the same humidity; thus, the two curves decline nearly in parallel. The green dashed line shows good agreement with the solid black line. The slight deviation is due to the delayed response in the evaporation process due to switching from one condition to another. During the whole evaporation process, the change rate of solute concentration evolves inversely proportional to the variation of volume. As shown in Figure 5c, this variation of the solutes in the DMEM leads to an increase of the pH value of the solution. We have additionally plotted the functional relationship of Rc_d versus V/V_0 in the Supporting Information: Figure S4. The interested readers are referred to the Supporting Information: Appendix section.

The pH level of the culture medium is a crucial factor that affects various cellular processes essential for promoting cell growth and survival. Changes in pH levels can affect nutrient solubility and availability, metabolic pathways, and protein folding, all of which are vital to cellular activities. By performing cellular assays in small droplets, even slight changes in volume generate a fluctuation in the concentration of metabolites and salts, leading to changes in pH levels. Therefore, precise monitoring of pH changes during the evaporation process is crucial to optimize cell culture conditions and to improve the performance of cell assays within droplets. In this study, we determined the pH of DMEM droplets containing a pH indicator without cells to obtain the pH value evolution during the whole evaporation process. In Figure 5b, the changes in the mean color intensity of DMEM droplets containing a pH indicator during the evaporation process were analyzed. The experiments for monitoring pH were conducted for droplets on a circular pattern (see the Supporting Information: Figure S1 for more details of the pattern). The measurement of the pH values and color intensity analysis was conducted for a single droplet that shows the same behavior as an individual droplet within an array with the droplet distance larger than the cutoff distance. The circular pattern was chosen for two specific reasons. First, the circular pattern facilitates a more uniform color image analysis compared to the square array because in the case of the square lattice, there is nonhomogeneous evaporation due to changes in the local curvature of the droplet, which also leads to local changes in the pH value. The second reason is that because the diameter is 1.4 mm, it

can accommodate a larger volume of liquid, providing a larger window for capturing high-quality images of the slides during the evaporation process. This allows us to capture more images during the evaporation process, providing us with a greater number of data points for analysis. We relate the pH value to the mean intensity with a fitting function: $pH = aM^2 + bM + m$ with $a = 6.30 \times 10^{-5}$, $b = 8.34 \times 10^{-3}$, and $m = 5.81$. Here, the variable M represents the mean intensity of the color (more details of the obtained results are presented in the Supporting Information: Table S1). Utilizing this functional correlation, we were able to trace the pH value changes of the droplets throughout the entire evaporation process in the experiment. The obtained pH value evolution is plotted in Figure 5c, where the inset shows the functional relationship between the droplet volume and the pH value. The volumes of the experimental droplets for pH value calculation were determined by measuring the height of the droplets during the experiment, which allows correlation of the real-time data of height with the mean intensity during the evaporation process. It is worth noting that we aim to propose a real-time method to track changes in the pH and solute concentration of a droplet that is closely linked to the volume change. The proposed method is applicable irrespective of whether the studied droplet is a single droplet or an individual droplet within a droplet array so long as the droplet volume is detectable.

CONCLUSION

In open parallelized and miniaturized platforms, for example, DMA, accurate volume control is crucial for high-throughput applications. In this work, we show that precise volume control of droplets can be achieved through a dedicate maneuvering of the evaporation process. We have experimentally and numerically explored the evaporation behavior of droplets on a DMA under various conditions by controlling the environmental humidity and temperature, as well as wetting properties. Remarkably, the phase-field simulations show excellent agreement with experiments for the evaporation of a single droplet and multiple droplets on a patterned substrate. Specifically, multiple droplets on surfaces with arrays of patterns (e.g., 4 × 4 or more) indicate nonuniform evaporation rates due to the locally nonuniformly distributed concentration of water vapor formed during the evaporation process, the so-called shielding effect. We further show that the shielding effect can be circumvented by increasing the droplet spacing and that the evaporation rate depends strongly on

the environmental humidity. Since the shielding effect slows down the evaporation and facilitates a stable culture environment, a quantitative description of volume evolution with time for an individual droplet within the droplet array in the presence of the shielding effect warrants an in-depth investigation. Some recent studies on this topic include the simulation work of Chong et al.[24] and the theoretical work of Masoud et al.,[26] in which they considered the collective evaporation behaviors of droplet arrays under the influence of the shielding effect.

To expand the scope of the phase-field approach for modeling the real evaporation process under the combined influence of humidity and temperature, we adopted an empirical equation that can be experimentally determined. Apart from the numerical model, we have also proposed a theoretical model to describe the shape of a droplet constrained on a noncircular pattern, which yields the functional relationship between the droplet volume and droplet height and thus simplifies the determination of droplet volume in experiments. This theoretical model can be easily extended to examine other topography-based wetting morphologies.

To assess the impact of evaporation on droplet composition during common laboratory procedures, we established a real-time method to track changes in the pH and solute concentration. Using DMEM culture medium as a proof of concept, we observed that the decrease in volume during an assays can cause a significant change in the pH and solute concentration; these changes not only have the potential to impact cell culture growth and stability but can also affect critical factors such as cell differentiation[48] and drug delivery,[49] among others, which are crucial aspects that need to be regulated in, for example, drug screening assays. Although our method was specifically tested on DMEM culture medium, it has potential applications for other compounds and even chemical reactions, providing a broad scope for the control of high-throughput miniaturized assays on DMA. However, further research is needed to address challenges such as the effects of pH levels on the physical properties of droplets and the impact of solute concentration on product formation in miniaturized synthesis reactions. Our study highlights the potential of establishing a digital twin system for miniaturized and parallelized applications that require real-time control of droplet behavior.

METHODS

The experiments were performed using chemically patterned microarrays (DMAs) from Aquarray on Schott Nexterion microscope slides. Two substrate formats were used: (1) rough glass slides with 1 mm^2 hydrophilic spots surrounded by superhydrophobic borders spaced 0.5 mm apart and (2) rough glass slides with circular spots 1.4 mm Ø surrounded by superhydrophobic borders spaced 2.2 mm apart (see the Supporting Information: Figure S1). The square spot array was chosen for the study of the evaporation behaviors of droplets because it is the standard array used in cell experimentation in our research group and it is most suitable for microscopy readouts due to

the square field of view. The four sides of the squares provide clear reference points for accurate positioning and alignment, ensuring consistency across multiple samples and facilitating the reproducibility of our experiments. Furthermore, as the development of this digital twin is intended to provide us with complete information about our system for applied use, it is crucial to begin our research by focusing on the ultimate long-term goal, which is a digital twin that can be used in assays on a 672 square spot array. Last but not the least, the surface area of a square array is higher than that of a circular spot array. The circular configurations are only used for the pH experiments.

DMA slides were purchased from Aquarray GmbH (Cat. No. G-np-102, G-dd-102, I-np-102, I-dd-102, I-dd-102 and Cat. No. G-np-202, G-dd-202, I-np-202, I-dd-202 on the website (for more details, please visit: https://www.aquarray.com/dma-slide). The surface fabrication method consists of first creating a rough coating based on nanoparticles functionalized with vinyl groups, which are subsequently functionalized either by hydrophilic or hydrophobic thiol via the thiol-ene photoclick reaction.

The respective liquids such as Dulbecco's buffered saline (DPBS), glycerol 5%, Dulbecco's modified eagle's medium (DMEM), NaCl (0.1, 2, and 5 M), and pure water were printed at desired volumes on the respective DMAs using the Certus flex liquid dispenser (Fritz Gyger AG).

Evaporation processes were observed using a KEYENCE Fluorescence Microscope BZ-X810 (Keyence Corporation) for top views and a Krüss DSA 25 contact angle goniometer for side views. ImageJ software (National Institutes of Health) was used to measure droplet heights and contact angles, with the scale based on the spot dimensions.

The temperature and humidity were measured using the DHT22 sensor (Adafruit Industries LLC) controlled by the Arduino UNO Rev3 microcontroller board (Arduino). The ambient relative humidity H and ambient temperature T are, respectively, $36 \pm 2\%$ and $25 \pm 1.2°C$, unless specified otherwise.

A pH scale (6.0–9.5) and sample (pH = 7.4) were prepared with DMEM without phenol red using Cresol red (Supelco Inc) by a Mettler Toledo FE20/EL20 pH Meter (Mettler Toledo). Afterward, the solutions were dispensed on 1.4 mm Ø spots DMA at a volume of 1.4 µL. Thereafter, the DMA was placed in a CanoScan8800F (Canon) to take an image of the pH scale and samples. The images have 3165 and 6178 pixels for width and height, respectively, and the horizontal and vertical resolutions are both 6400 dpi. The scanning speeds for 300 and 4800 dpi are 1.0 and 12.1 ms/line, respectively. Next, the DMA was left to evaporate inside the scanner and images of this process were taken every 5 min. Finally, the intensity of the color for the evaporating droplet was measured using Gridscreener software,[50] which allows determination of the correlation of the initial color's mean intensity of the pH scale with the mean intensity variation of the samples upon evaporation. In parallel, a replicate of the same test was monitored using a goniometer to measure the evaporating droplet height at each point. The humidity and temperature inside the scanner and the goniometer were monitored using the DHT22 sensor.
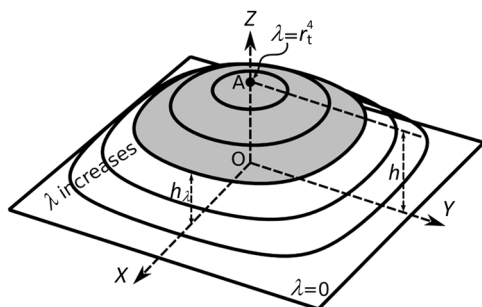
FIGURE 6 Schematic of the equilibrium droplet shape on a square-patterned substrate in a three-dimensional coordinate system ($OXYZ$). The liquid–gas interface is described by a series of contour lines. The point A highlights the apex of the droplet and h shows the droplet height.

We describe the liquid–gas interface with a series of contour curves obtained by cutting the droplet cap with flat surfaces parallel to the droplet base, as shown in Figure 6. When $h_\lambda = 0$, the contour curve approaches a square, while as h_λ increases, the curves become smoother and rounder, becoming circular near the apex of the droplet. We construct a mathematical formulation of these contour curves as follows:

$$(y - r_t)(y + r_t)(x - r_t)(x + r_t) - \lambda = 0. \quad (2)$$

The parameter r_t is the radius of the inner tangent circle of the square pattern. The parameter ($\lambda \in [0, \lambda_{max}]$) controls the roundness of the curve, which is related to the height $h_\lambda (h_\lambda \in [0, h])$, as proposed in the equation $h_\lambda(\lambda) = h_\lambda / \lambda_{max}$. The parameter h represents the droplet height and $\lambda_{max} = r^4$ is the maximum value of λ. The droplet volume is calculated using $V = \int_0^h A(h_\lambda) dh_\lambda$, $A(h_\lambda)$ denoting the surface area for the droplet cross-section on height h_λ. For a certain V and a certain base pattern, h can be determined. In sum, $h_\lambda(\lambda)$ and Equation (2) can be used to identify the 3D droplet shape.

We consider the evaporation kinetics of multiple sessile droplets of pure fluids on nonheated surfaces. The different liquids and solutions are treated as pure fluids with certain volatilities. To model such a two-phase system, the order parameter c is introduced to characterize the phase state. The free-energy functional of the system $F(J)$ is written as

$$F = \int_\Omega [f(c) + 2\sigma\epsilon (\nabla c)^2] d\Omega, \quad (3)$$

where Ω (m^3) is the spatial domain and ϵ (m) is the interface width. σ (N/m) is related to the surface energy density.

The free-energy density f is

$$f(c) = \left(\frac{\sigma}{\epsilon}\right)[c \ln c + (1 - c)\ln(1 - c) + Xc(1 - c)]. \quad (4)$$

The parameter X indicates an interaction coefficient between the two components. This is a double-well function with energy minima $(c_{e1}, f(c_{e1}))$ and $(c_{e2}, f(c_{e2}))$. The order parameters c_{e1} and c_{e2} denote the two equilibrium order parameters and fulfill $f'(c_{e1}) = f'(c_{e2}) = 0$.

The CH equation is given as

$$\partial c/\partial t = \nabla \cdot [(\epsilon/\sigma)D_e c(1 - c)\nabla(\delta F/\delta c)], \quad (5)$$

where D_e is the effective diffusion coefficient.

At the substrate, the following boundary condition at the fluid–substrate interface[51,52] is set:

$$4\sigma\epsilon \nabla c \cdot \boldsymbol{n} - (\gamma_{gs} - \gamma_{ls})l'(c) = 0, \quad (6)$$

with liquid–gas surface tension $\gamma_{lg} = \sigma$ and $l(c)$ denoting an interpolation function that fulfills $l(c_{e1}) = 0$, $l(c_{e2}) = 1$, and $l'(c_{e1}) = l'(c_{e2}) = 0$. The notation $\boldsymbol{n}$ represents the inward pointing normal vector of the solid substrate. The parameters γ_{ls} (N/m) and γ_{gs} (N/m) are, respectively, the interfacial tensions of the liquid–solid and gas–solid interfaces. This boundary condition has been validated in previous work for simulating the equilibrium shape of droplets on chemically patterned substrates.[33,34,39] The current model is capable of modeling a combined wetting effect and evaporation process by choosing appropriate boundary conditions.

CONFLICT OF INTEREST STATEMENT

The authors declare the following potential conflicts of interest with respect to the research, authorship, and/or publication of this article: in addition to being employed by the Karlsruhe Institute of Technology, Anna A. Popova and Pavel A. Levkin are (since March 2018) shareholders of Aquarray GmbH. The remaining authors declare no conflict of interest.

ORCID

Yanchen Wu http://orcid.org/0000-0003-0636-5089
Joaquin E. Urrutia Gomez http://orcid.org/0000-0001-5411-9689

REFERENCES

1. Bonn D, Eggers J, Indekeu J, Meunier J, Rolley E. Wetting and spreading. *Rev Mod Phys.* 2009;81:739-805.
2. Brutin D, Starov V. Recent advances in droplet wetting and evaporation. *Chem Soc Rev.* 2018;47:558-585.
3. Wang Z, Orejon D, Takata Y, Sefiane K. Wetting and evaporation of multicomponent droplets. *Phys Rep.* 2022;960:1-37.
4. Kim S, Wu Z, Esmaili E, Dombroskie JJ, Jung S. How a raindrop gets shattered on biological surfaces. *Proc Natl Acad Sci USA.* 2020;117: 13901-13907.
5. Chen D, McKinley GH, Cohen RE. Spontaneous wettability patterning via creasing instability. *Proc Natl Acad Sci USA.* 2016;113: 8087-8092.
6. Soltani M, Golovin K. Lossless, passive transportation of low surface tension liquids induced by patterned omniphobic liquidlike polymer brushes. *Adv Funct Mater.* 2022;32:2107465.

7. Squires TM, Quake SR. Microfluidics: fluid physics at the nanoliter scale. *Rev Mod Phys*. 2005;77:977-1026.

8. Seemann R, Brinkmann M, Pfohl T, Herminghaus S. Droplet based microfluidics. *Rep Prog Phys*. 2011;75:016601.

9. Lohse D. Fundamental fluid dynamics challenges in inkjet printing. *Annu Rev Fluid Mech*. 2022;54:349-382.

10. Wang Y, Jin R, Shen B, et al. High-throughput functional screening for next-generation cancer immunotherapy using droplet-based microfluidics. *Sci Adv*. 2021;7:eabe3839.

11. Wang F, Wu Y, Nestler B. Wetting effect on patterned substrate. *Adv Mater*. 2023;35:2210745.

12. Ren J, Duan F. Recent progress in experiments for sessile droplet wetting on structured surfaces. *Curr Opin Colloid Interface Sci*. 2021;53:101425.

13. Kang SM, You I, Cho WK, et al. One-step modification of superhydrophobic surfaces by a mussel-inspired polymer coating. *Angew Chem Int Ed*. 2010;49:9401-9404.

14. Darmanin T, de Givenchy ET, Amigoni S, Guittard F. Super-hydrophobic surfaces by electrochemical processes. *Adv Mater*. 2013;25:1378-1394.

15. Ma M, Mao Y, Gupta M, Gleason KK, Rutledge GC. Super-hydrophobic fabrics produced by electrospinning and chemical vapor deposition. *Macromolecules*. 2005;38:9742-9748.

16. Feng W, Ueda E, Levkin PA. Droplet microarrays: from surface patterning to high-throughput applications. *Adv Mater*. 2018;30:1706111.

17. Wiedmann JJ, Demirdögen YN, Schmidt S, et al. Nanoliter scale parallel liquid–liquid extraction for high-throughput purification on a droplet microarray. *Small*. 2023;19:2204512.

18. Neto AI, Levkin PA, Mano JF. Patterned superhydrophobic surfaces to process and characterize biomaterials and 3D cell culture. *Mater Horizons*. 2018;5:379-393.

19. Khilifi D, Foudhil W, Fahem K, Harmand S, Ben J. Study of the phenomenon of the interaction between sessile drops during evaporation. *Ther Sci*. 2019;23:1105-1114.

20. Hatte S, Pandey K, Pandey K, Chakraborty S, Basu S. Universal evaporation dynamics of ordered arrays of sessile droplets. *J Fluid Mech*. 2019;866:61-81.

21. Schofield FGH, Wray AW, Pritchard D, Wilson SK. The shielding effect extends the lifetimes of two-dimensional sessile droplets. *J Eng Math*. 2020;120:89-110.

22. Wray AW, Duffy BR, Wilson SK. Competitive evaporation of multiple sessile droplets. *J Fluid Mech*. 2020;884:A45.

23. Wray AW, Wray PS, Duffy BR, Wilson SK. Contact-line deposits from multiple evaporating droplets. *Phys Rev Fluids*. 2021;6:073604.

24. Chong KL, Li Y, Ng CS, Verzicco R, Lohse D. Convection-dominated dissolution for single and multiple immersed sessile droplets. *J Fluid Mech*. 2020;892:A21.

25. Edwards AMJ, Cater J, Kilbride JJ, et al. Interferometric measurement of co-operative evaporation in 2D droplet arrays. *Appl Phys Lett*. 2021;119:151601.

26. Masoud H, Howell PD, Stone HA. Evaporation of multiple droplets. *J Fluid Mech*. 2021;927:R4.

27. Chen H, An Q, Zhang H, Li C, Fang H, Yin Z. Predicting the lifetimes of evaporating droplets in ordered arrays. *Phys Fluids*. 2022;34:082010.

28. Nguyen TAH, Nguyen AV. On the lifetime of evaporating sessile droplets. *Langmuir*. 2012;28:1924-1930.

29. Stauber JM, Wilson SK, Duffy BR, Sefiane K. On the lifetimes of evaporating droplets. *J Fluid Mech*. 2014;744:R2.

30. Hu H, Larson RG. Evaporation of a sessile droplet on a substrate. *J Phys Chem B*. 2002;106:1334-1344.

31. Wilson SK, D'Ambrosio HM. Evaporation of sessile droplets. *Annu Rev Fluid Mech*. 2023;55:481-509.

32. Sáenz PJ, Wray AW, Che Z, et al. Dynamics and universal scaling law in geometrically-controlled sessile drop evaporation. *Nat Commun*. 2017;8:14783.

33. Wu Y, Wang F, Selzer M, Nestler B. Droplets on chemically patterned surface: a local free-energy minima analysis. *Phys Rev E*. 2019;100:041102.

34. Wu Y, Wang F, Ma S, Selzer M, Nestler B. How do chemical patterns affect equilibrium droplet shapes? *Soft Matter*. 2020;16:6115-6127.

35. Cahn JW, Hilliard JE. Free energy of a nonuniform system. I. Interfacial free energy. *J Chem Phys*. 1958;28:258-267.

36. Hohenberg PC, Halperin BI. Theory of dynamic critical phenomena. *Rev Mod Phys*. 1977;49:435-479.

37. Lacasta AM, Sokolov IM, Sancho JM, Sagués F. Competitive evaporation in arrays of droplets. *Phys Rev E*. 1998;57:6198-6201.

38. Wu Y, Wang F, Selzer M, Nestler B. Investigation of equilibrium droplet shapes on chemically striped patterned surfaces using phase-field method. *Langmuir*. 2019;35:8500-8516.

39. Wu Y, Kuzina M, Wang F, et al. Equilibrium droplet shapes on chemically patterned surfaces: theoretical calculation, phase-field simulation, and experiments. *J Colloid Interface Sci*. 2022;606:1077-1086.

40. Wang F, Zhang H, Wu Y, Nestler B. A thermodynamically consistent diffuse interface model for the wetting phenomenon of miscible and immiscible ternary fluids. *J Fluid Mech*. 2023;970:A17.

41. Ewetola M, Ledesma-Aguilar R, Pradas M. Control of droplet evaporation on smooth chemical patterns. *Phys Rev Fluids*. 2021;6:033904.

42. Cazabat AM, Guéna G. Evaporation of macroscopic sessile droplets. *Soft Matter*. 2010;6:2591-2612.

43. Semenov S, Trybala A, Rubio RG, Kovalchuk N, Starov V, Velarde MG. Simultaneous spreading and evaporation: recent developments. *Adv Colloid Interface Sci*. 2014;206:382-398.

44. Hirschefelder J, Curtiss CF, Bird RB. *Molecular Theory of Gases and Liquids*. Wiley; 1954.

45. Sherwood TK, Pigford RL, Wilke CR, et al. *Mass Transfer*. McGraw-Hill; 1975.

46. Mostinsky IL. *Diffusion Coefficient. A-to-Z Guide to Thermodynamics, Heat and Mass Transfer, and Fluids Engineering*. Thermopedia powered by TrendMD; 2011.

47. McCabe WL, Smith JC, Harriott P. *Unit Operations of Chemical Engineering*. McGraw-Hill; 1993.

48. McAdams TA, Miller WM, Papoutsakis ET. Variations in culture pH affect the cloning efficiency and differentiation of progenitor cells in ex vivo haemopoiesis. *Br J Haematol*. 1997;97:889-895.

49. Madhusudhan A, Reddy G, Venkatesham M, et al. Efficient pH dependent drug delivery to target cancer cells by gold nanoparticles capped with carboxymethyl chitosan. *Int J Mol Sci*. 2014;15:8216-8234.

50. Schilling MP, Schmelzer S, Gomez JEU, Popova AA, Levkin PA, Reischl M. Grid screener: a tool for automated high-throughput screening on biochemical and biological analysis platforms. *IEEE Access*. 2021;9:166027-166038.

51. Jacqmin D. Contact-line dynamics of a diffuse fluid interface. *J Fluid Mech*. 2000;402:57-88.

52. Ding H, Spelt PDM. Wetting condition in diffuse interface simulations of contact line motion. *Phys Rev E*. 2007;75:046708.

SUPPORTING INFORMATION

Additional supporting information can be found online in the Supporting Information section at the end of this article.